JOURNAL OF PROPULSION AND POWER
Vol. 16, No. 2, March–April 2000

Time-Accurate Three-Dimensional Navier–Stokes Analysis of One-and-One-Half Stage Axial-Flow Turbine

Thomas W. Volmar,* Bernard Brouillet,† and Heinz E. Gallus‡
Institut für Strahlantriebe und Turboarbeitsmaschinen, D-52062 Aachen, Germany
and
Hannes Benetschik§
AEA Technology GmbH, D-83624 Otterfing, Germany

A new three-dimensional Navier–Stokes method for the analysis of the unsteady flow in multiple turbomachinery blade rows is presented. To take into account turbulent effects, a low-Reynolds-number k–ϵ model is used. Smooth wave propagation accross the sliding rotor/stator interfaces is accomplished with a fully conservative interface flux algorithm. The use of physically motivated time-step scales is enabled by an implicit relaxation strategy, where Newton subiterations are applied to provide time accuracy. The code system is validated for a one-and-one-half-stage axial-flow turbine, which is documented as an ERCOFTAC SIG test case. Detailed experimental data are exploited to evaluate the predictive capability of the code. The analysis focuses on typical unsteady effects such as negative jets in the wakes, general effects of unsteadiness, as well as the representation and the unsteady generation of losses.

Introduction

TURBOMACHINERY flows are inherently three-dimensional and unsteady. The latter is because of a variety of reasons, the most important of which are time dependencies of inflow and outflow conditions, blade flutter phenomena, and finally, the interaction between fixed and moving blade rows. During the last decade, isolated blades or blade rows respectively have been the objective of a vast number of investigations. Detailed experimental data were thoroughly exploited for a profound validation of numerical computations. As unsteadiness is recognized to play a key role in loss generation, the predictive limitations of single-blade-row analyses are obvious. To minimize size and weight of modern gas turbines, axial gaps between blade rows are decreased, which in turn increases rotor/stator interaction. Typical blade-row interaction-induced phenomena may be summarized as follows:

1) The influence of potential flow: acoustic waves travel in any, e.g., upstream, direction.

2) Off-design inlet conditions of downstream blade rows: blade wakes periodically induce off-design incidences for downstream blade rows, thereby introducing pressure fluctuations.

3) The influence of secondary vortical flow.

4) Deformation of wakes and vortices caused by inhomogeneous velocity fields.

5) Increasing turbulence in downstream blade rows.

6) Wake-induced laminar/turbulent transition.

7) Turbulent diffusion increases the energy level in the boundary layers, where the susceptibility to separation is decreased.

8) The influence of unsteadiness on heat transfer at the blade surface.

9) Blade oscillation caused by unsteady pressure including excitation and fatigue.

Because of a three-dimensional unsteady flowfield structure, local acceleration assumes a nonnegligible amount of the convective acceleration. The associated ratio of accelerations is usually represented by the so-called reduced frequency, which assumes values of an order of magnitude of 10 and higher.

The most simplistic way of simulating rotor/stator interaction for an isolated blade row involves the use of time periodic boundary conditions, where wakes of upstream blade rows are taken into account.[1] Such methods provide sufficient capacity to investigate transport and deformation of wakes subject to the single blade-row flowfield.

A very popular approach involves establishing a mixing plane between the blade rows by more or less sophisticated ways of averaging the flow quantities in circumferential direction. Thus, the entire flowfield can be assumed to be steady.[2] Thereby, computational requirements are reduced by orders of magnitude compared to a time-accurate simulation. On the other hand, many details of the interaction are lost by this simplification, in particular unsteady features. Mixing-plane methods mask physical flow details and are therefore not suitable for getting a thorough understanding of loss generation caused by the rotor/stator interaction. However, various global parameters can be simulated well as mentioned in Ref. 2.

The most refined mixing-plane approach known so far was introduced by Adamczyk et al.[3] According to the idea of Reynolds for turbulent flows, the periodically unsteady flow is decomposed into a mean value and a periodic deviation. Although computational efficiency is high, numerous empirical assumptions are required.

To accomplish true transient simulations of the interaction, several simplifications of the governing equations are in use, e.g., the potential flow model,[4] the inviscid Euler equations,[5] or the Navier–Stokes equations with complex turbulence models.[6] Simulations are realized in two and three spatial dimensions.

Depending on the degree of simplification, more or less interactive features may be examined. Because many of these unsteady phenomena are of three-dimensional and of viscous nature (see points just listed), the present analysis applies a time-accurate solution of the complete set of three-dimensional Navier–Stokes equations with a k–ϵ turbulence model. The new code is an extension of the single blade-row analysis code detailed in Ref. 7, where significant code revisons and extension are introduced. Computational results presented herein reflect the time evolution of the flow in a one-and-one-half-stage axial-flow turbine, where low-blade aspect ratios cause a high degree of three dimensionality.

Governing Equations

The Favre-averaged Navier–Stokes equations along with the k–ϵ turbulence model are initially cast into a Cartesian coordinate system

Received 28 September 1998; revision received 23 March 1999; accepted for publication 14 April 1999.

*Research Engineer, Templergraben 55, RWTH; currently with RWE Energie AG Essen, Germany.
†Research Engineer, Templergraben 55, RWTH; currently with MTU Motoren- und Turbinen-Union München GmbH, Germany.
‡Professor, Director of the Institute, Templergraben 55, RWTH.
§CFD Consulting Engineer, Staudenfeldweg 12.

rotating about the x axis at an angular velocity Ω and then transformed into a body-fitted coordinate system.[7] By virtue of the tensor notation, the resulting set of equations reads

$$\sqrt{g}\frac{\partial \rho}{\partial t} + \frac{\partial\left[\sqrt{g}(\partial \xi^j/\partial x^k)\rho w_x^k\right]}{\partial \xi^j} = 0 \tag{1}$$

$$\sqrt{g}\frac{\partial \rho c_x^i}{\partial t} + \frac{\partial\left[\sqrt{g}(\partial \xi^j/\partial x^k)\left(\rho c_x^i w_x^k + p\delta^{ik}\right)\right]}{\partial \xi^j} = \frac{\partial\left[\sqrt{g}(\partial \xi^j/\partial x^k)\sigma_x^{ik}\right]}{\partial \xi^j} + \sqrt{g}\epsilon_{klm}\rho c_x^k \Omega^l \delta^{im} \tag{2}$$

$$\sqrt{g}\frac{\partial \rho e_{\text{rot}}}{\partial t} + \frac{\partial\left[\sqrt{g}(\partial \xi^j/\partial x^k)(\rho e_{\text{rot}} + p)w_x^k\right]}{\partial \xi^j} = \frac{\partial\left[\sqrt{g}(\partial \xi^j/\partial x^k)\left(\sigma_x^{kl} w_x^l + q_x^k\right)\right]}{\partial \xi^j} \tag{3}$$

$$\sqrt{g}\frac{\partial \rho k}{\partial t} + \frac{\partial\left[\sqrt{g}(\partial \xi^j/\partial x^k)\rho k w_x^k\right]}{\partial \xi^j} = \frac{\partial\left[\sqrt{g}(\partial \xi^j/\partial x^k)\mu_k(\nabla k)_x^k\right]}{\partial \xi^j} + \sqrt{g}(P - \rho\epsilon - F_1) \tag{4}$$

$$\sqrt{g}\frac{\partial \rho \epsilon}{\partial t} + \frac{\partial\left[\sqrt{g}(\partial \xi^j/\partial x^k)\rho\epsilon w_x^k\right]}{\partial \xi^j} = \frac{\partial\left[\sqrt{g}(\partial \xi^j/\partial x^k)\mu_\epsilon(\nabla \epsilon)_x^k\right]}{\partial \xi^j} + \sqrt{g}\left(\frac{\epsilon}{k}\left(f_1 c_{\epsilon_1} P - f_2 c_{\epsilon_2}\rho\epsilon\right) - F_2\right) \tag{5}$$

In these equations ρ denotes the density, p the pressure, and c_x^i, w_x^i are the absolute and relative Cartesian velocity components, respectively. Assuming an ideal gas, the modified total energy in the rotating frame of reference e_{rot} is defined as follows:

$$e_{\text{rot}} = \frac{p}{\gamma - 1} + \rho\frac{\left(c_x^i\right)^2}{2} - \rho\epsilon_{klm}\Omega^k x^l \delta^{im} c_x^i - \frac{5 - 3\gamma}{3(\gamma - 1)}\rho k \tag{6}$$

where γ is the ratio of specific heats. The components of the stress tensor, the heat fluxes, and the gradient of turbulence quantities follow the assumptions of Stokes, Fourier, Reynolds, Favre, and Boussinesq. Details of the k–ϵ turbulence model such as the empirical constants and improvements for the viscous sublayers (low-Reynolds-number variant by Chien) can be found in Ref. 8. An approach to improve stagnating flows is outlined in Ref. 7, according to Ref. 9. To take into account the convective character of turbulence, the simulation of rotor/stator interaction can be expected to yield superior results by virtue of a multi-equation turbulence model compared to algebraic models.

Discretization in Space and Time

Basic Scheme

The solution to the set of equations is realized in a cell-centered finite-volume framework. The numerical algorithm uses a higher-order upwind-biased approximation of the inviscid fluxes with an approximate Riemann solver. To take into account the wave-like nature of the convective parts of the equations, Roe's flux-difference-splitting technique[10] is used. Details of the present implementation are given in Ref. 7. Viscous terms are discretized according to Chakravarthy,[11] where cross derivatives contribute to diagonal dominance. To realize numerical stability with a time step being motivated by physical timescales of the rotor/stator interaction rather than by a stability condition, the simulation is advanced in time implicitly.

Within the implicit algorithm solving for the conserved quantities $\boldsymbol{Q}$, the inviscid fluxes $\boldsymbol{F}$, the viscous fluxes $\boldsymbol{S}$, and the source terms $\boldsymbol{H}$ are assumed to be known at the new time level $n + 1$

$$\underbrace{\sqrt{g}\frac{\boldsymbol{Q}_{i,j,k}^{n+1} - \boldsymbol{Q}_{i,j,k}^{n}}{\Delta t} + \sum_{l=1}^{3}\Delta \boldsymbol{F}_\xi^l(\boldsymbol{Q}^{n+1}) - \sum_{l=1}^{3}\Delta \boldsymbol{S}_\xi^l(\boldsymbol{Q}^{n+1}) - \boldsymbol{H}(\boldsymbol{Q}^{n+1})}_{f(\boldsymbol{Q}^{n+1}) = 0_{i,j,k}} \tag{7}$$

where the Δ operator denotes the flux balance of the control volume i, j, k. Equation (7) is a nonlinear system of equations for the unknown $\boldsymbol{Q}^{n+1}$, which is solved by Newton subiterations, with the iteration count being denoted as p:

$$\frac{\partial \boldsymbol{f}}{\partial \boldsymbol{Q}}\left[\boldsymbol{Q}^{n+1(p)}\right] \cdot \left[\boldsymbol{Q}^{n+1(p+1)} - \boldsymbol{Q}^{n+1(p)}\right] = -\boldsymbol{f}\left[\boldsymbol{Q}^{n+1(p)}\right] \tag{8}$$

To enhance time accuracy, several Newton iterations are performed at each time step. The linear system underlying each Newton iteration is solved by a block-Gauss–Seidel iterative algorithm thus involving LU inversions of the local 7×7 blocks. An alternating block-line relaxation scheme is implemented as well, see Ref. 7. Because the overall efficiency has not been found to significantly outperform the block-Gauss–Seidel algorithm, it has not been used in the present investigation.

Equation (7) is only of first-order accuracy in time. To achieve second-order time accuracy, the two-point transient discretization is replaced by a three-point formula, cf. Ref. 12:

$$\frac{\partial \boldsymbol{Q}_{i,j,k}}{\partial t} = \frac{3\boldsymbol{Q}_{i,j,k}^{n+1} - 4\boldsymbol{Q}_{i,j,k}^{n} + \boldsymbol{Q}_{i,j,k}^{n-1}}{2\Delta t} = \frac{3}{2}\frac{\boldsymbol{Q}_{i,j,k}^{n+1} - \boldsymbol{Q}_{i,j,k}^{n}}{\Delta t} - \frac{1}{2}\frac{\boldsymbol{Q}_{i,j,k}^{n} - \boldsymbol{Q}_{i,j,k}^{n-1}}{\Delta t} \tag{9}$$

The use of the preceding relation does not introduce any computational penalty, but memory requirements increase because of an additional data storage level $n - 1$.

Boundary Conditions

At solid walls the no-slip condition is enforced, assuming vanishing normal pressure and temperature gradients. According to Ref. 8, both k and ϵ are set to zero.

At inflow and outflow boundaries the Riemann invariants are prescribed, the magnitude of which is obtained from previous steady-state computations. At inflow entropy p/ρ^γ, tangential velocity components k, ϵ, and the acoustic Riemann invariant $\hat{w}_\perp - 2a/(\gamma - 1)$ are specified, where $\hat{w}_\perp$ denotes the normal velocity component and a is the local speed of sound. At outflow boundaries the upstream running acoustic Riemann invariant $\hat{w}_\perp + 2a/(\gamma - 1)$ is imposed.

Within the framework of a complete stage computation where the blade counts in each row are different, periodic boundaries are to be considered in space time, as a purely spatial periodicity no longer holds between adjacent blades. Using the time lag ΔT between adjacent blades, the spatially and temporally shifted boundaries are defined according to Erdos et al.[13] Upon denoting the circumferential angular position by φ, the periodic boundary condition takes the form if $\Delta T \geq 0$

$$\begin{aligned} Q(x, \varphi, t) &= Q(x, \varphi - \Delta\varphi_{\text{pitch}}, t - \Delta T) \\ Q(x, \varphi, t) &= Q(x, \varphi + \Delta\varphi_{\text{pitch}}, t + \Delta T - T_A) \end{aligned} \tag{10}$$

where T_A denotes the time period of blade row A under consideration. Therefore, the values at the periodic boundaries must be stored in time for a whole period leading to significantly increased memory requirements.

At the sliding blade-row interface relative motion is taken into account. Thus, computational interface cells are opposed to temporally varying and, in general, to several adjacent flux cells. To achieve a

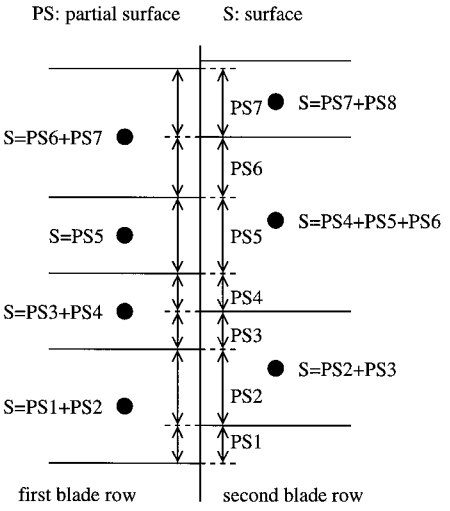

Fig. 1 Blade-to-blade view of the sliding interface approach.

locally conservative formulation, a partial surface concept is used, as shown in Fig. 1.

At each time step the sets of contacting cells are determined. To accomplish coincidence among contacting flux cells, partial cell faces and fluxes are computed. Finally, partial fluxes are assembled to yield a fully conservative flux balance for each cell located at the sliding interface. Thus, the present approach is similar to the technique detailed in Ref. 2. Because of the time shift, quantities at the interface are to be stored in memory as mentioned for the periodic boundaries.

Test Facility

The measurements have been conducted in a one-and-one-half-stage cold-air turbine, which has been designed and built at the Institut für Strahlantriebe of the Technical University of Aachen. The geometry, blade counts, and stagger are identical. Therefore, the time lag ΔT caused by the different blade counts between the rotor (41 blades) and the stators (36 blades) is unique in any point of the turbomachine. Accordingly, the space-time periodicity method by Erdos et al.[13] can be used for the present three-cascade configuration. Further details of the geometry and the flow conditions can be found in the ERCOFTAC SIG Testcase U1 (Ref. 14).

Here, steady as well as unsteady measurements in hub-to-shroud planes at three axial locations (first stator exit, rotor exit, second stator exit) are available. The steady measurements are conducted by pneumatic probes; unsteady data are obtained by means of a triple hot-wire probe. The measurements have been realized at 20 positions in radial direction and 17 positions in circumferential direction, thereby generating several snapshots of each plane.

Grid System

The present rotor-stator configuration is discretized using O-type grids for each cascade. Inside the rotor-tip clearance region, an internal O-type grid involving a singular center is patched into the primary cascade O-type grid. The complete grid-generation procedure for every single cascade is detailed in Ref. 7. Here, 36 spanwise surfaces of revolution are generated to serve the elliptic quasi-three-dimensional blade-to-blade grid-generation procedure. Figure 2 depicts the gridding of the turbine at a midspan section and in the rotor tip clearance. With respect to a homogeneous inflow, the first stator grid is the least dense of all with 115×27 points being used on each blade-to-blade section. To maintain a continuous global grid density, more nodes are required to discretize the rotor blade-to-blade sections. Here, 145×31 nodes are introduced. As no unsteady interaction is expected downstream of the stage, some grid coarsening is adequate for the second stator grid, which consists of 127×31 nodes on each spanwise section. Finally, the rotor-tip clearance grid comprises $145 \times 15 \times 6$ nodes resulting in a total number of 428382 grid nodes.

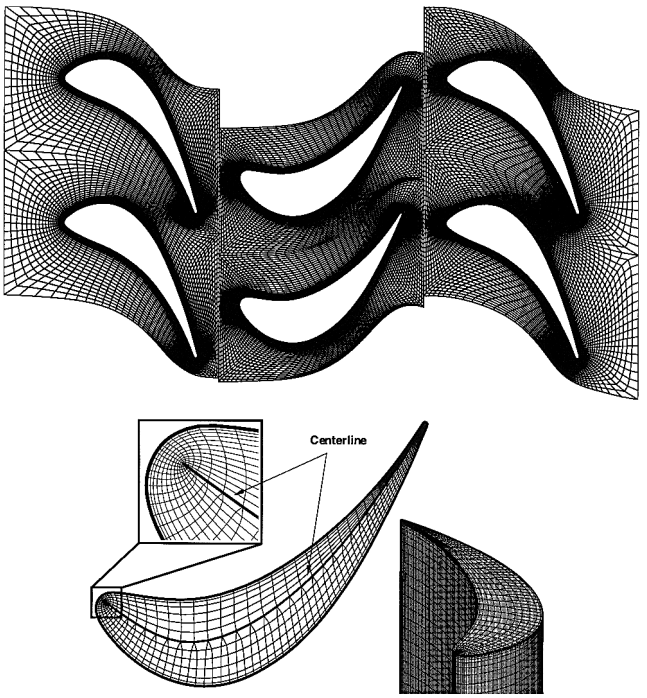

Fig. 2 Computational grid at midspan and inside rotor-tip clearance.

Results

Basic Characteristics

The use of time-shifted periodicity conditions is essential to this technique, which therefore requires the computation of several periodic cycles until convergence is achieved. In the present study ten blade-passing cycles were found to provide good convergence, where every cycle was resolved by about 100 time steps. To provide time accuracy, three Newton subiterations have been computed. Within each subiteration 10 Gauss–Seidel relaxation sweeps were performed to solve the system of linear equations.

Integral Quantities

Mach numbers, total pressures, and yaw angles may be mass averaged over the three axial gap surfaces (in addition to the inflow plane) and compared to their experimental equivalents. Unfortunately, experimental data are reported to exhibits light inconsistencies.[14,15] In particular, the inlet Mach number, which was underlying the measurements in the different axial gap surfaces, has been found to range between $Ma_0 = 0.12 \pm 0.05$. This fact is caused by measuring the flow data during different measurement campaigns. Therefore a perfect matching between experiment and computation cannot be expected.

The experimental mass-flow rate covers the range between 6.5 up to 6.7 kg/s, whereas the computed value is 7.0 kg/s. Thus, the computed value is about 4% higher than the experimental ones, which is below the range of uncertainty of experimental data.

Figure 3 compares the integral quantities in all measuring planes, that is, in front of, between, and behind the blade rows. As can be seen, the computed inflow Mach number is 0.13, which is slightly higher than the average of 0.12 out of the set of experimental data. At this stage the underprediction of the first stator exit Mach number is emphasized, indicating the importance of transition modeling at least in the first blade row. The present computation assumes a fully turbulent flow. Especially in turbine flows, this assumption is not very realistic. Transition modeling is not taken into account here, leading to the overprediction of losses. From Fig. 3 the conclusion can be made that the effect of transition within the rotor and the second stator is less pronounced because of the increased freestream turbulence intensity.

Total pressure losses are generally slightly overpredicted, which can be traced back to various reasons, such as grid dependency

and/or no transition modeling. As can be seen from Fig. 3, the prediction of flow angles is excellent in either plane.

Temporally and circumferentially averaged yaw angles compare well to experimental data except for the end-wall regions of the rotor exit (see Fig. 4). Because computational results fit measurements well at the second stator exit, different probe types in the stator and rotor exit planes near the end walls largely increase experimental uncertainty locally. The latter assumption is supported by flowfield measurements in the forthcoming section.

Characteristic Details

The purpose of the current subsection is to illustrate details that are not restricted to an unsteady flowfield. Figure 5 depicts streamlines at the first stator leading edge close to the hub. First one can see that the adverse pressure gradient at the leading edge caused by sufficiently high mean flow kinetic energy and second the less pronounced static pressure rise in low kinetic energy end-wall flow onsets both local boundary-layer separation and horseshoe vortex roll up at the leading edge.

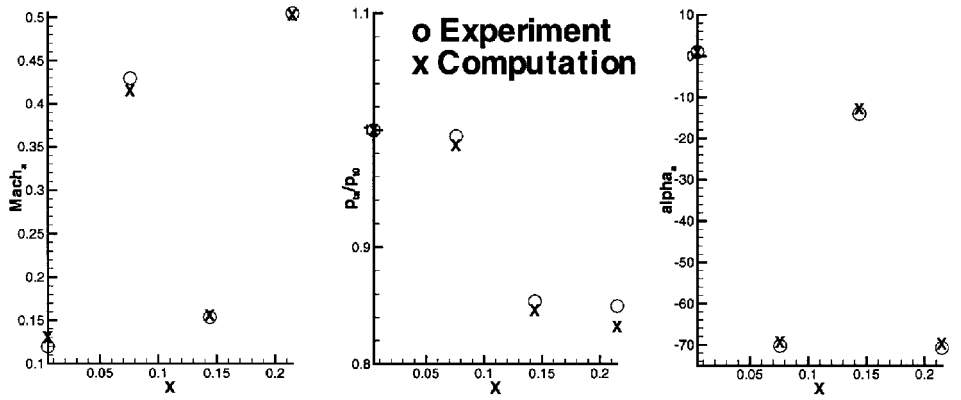

Fig. 3 Comparison between computation and experiment: mass-averaged quantities at experimental axial stations.

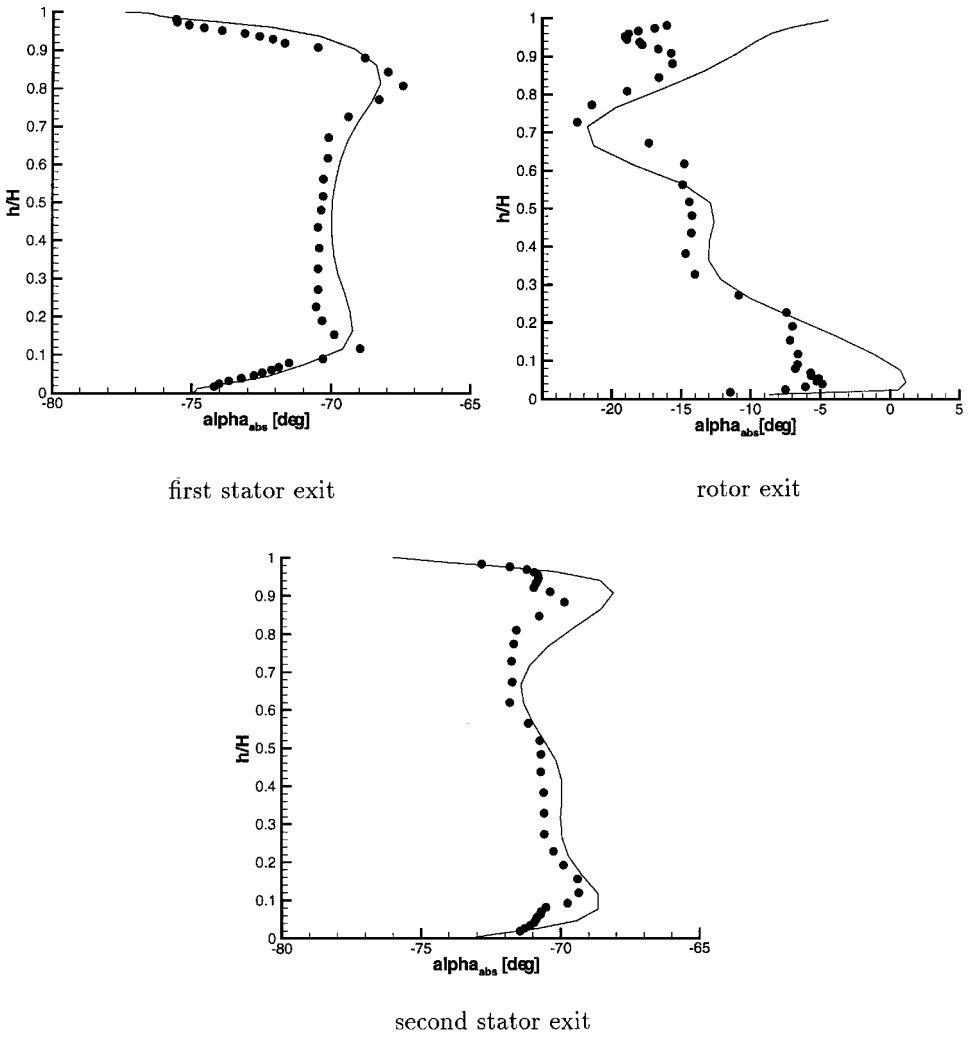

Fig. 4 Temporally and circumferentially averaged yaw angles at three experimental axial stations: ——, computation, and ●, experiment.

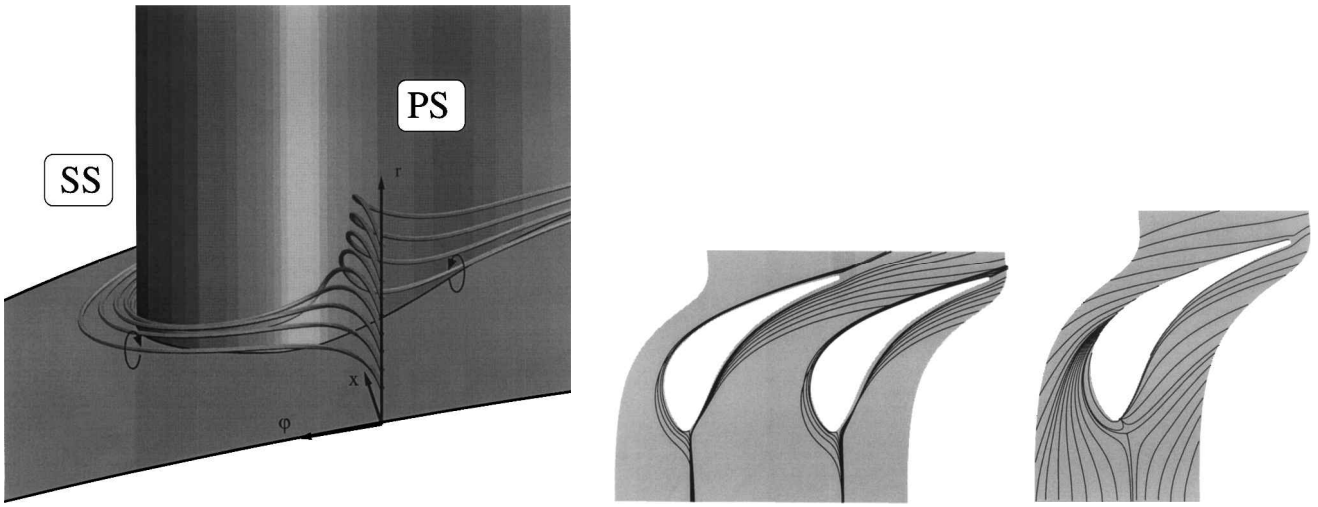

a) Spatial view

b) Planar hub projection of streamlines according to a)

c) Wall streamlines at hub

Fig. 5 Horseshoe vortex formation at the first stator leading edge near hub.

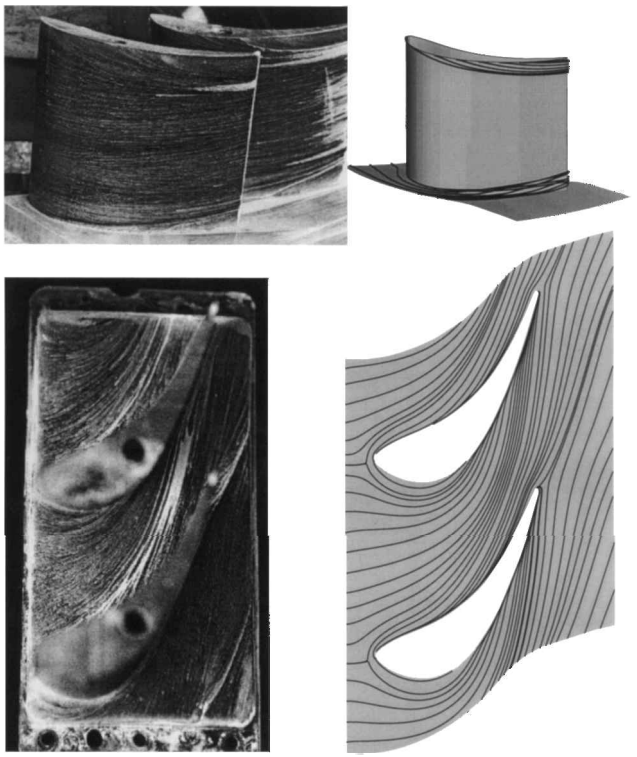

Fig. 6 Comparison between oilflow pattern (left column)[16] and computed streamlines (right column); first stator.

Interaction as well as merging of the horseshoe vortex and the shroud passage vortex are illustrated in Fig. 6. Here, the second stator blades are mounted on the casing and depict the oil-flow traces on the shroud and the blade surfaces. Computational results are seen to be in close agreement with experimental flow visualization. The cascade flowfield is highly three-dimensional, as the horseshoe/shroud passage vortex system is deflected toward the blade suction side, where it leads to a significant increase in boundary-layer displacement.

The rotor flowfield exhibits additional complexity because of the tip clearance flow. Unlike a compressor tip clearance flow pattern, relative casing motion counteracts the pressure gradient. From Fig. 7 one can obviously see that the effect of the spinning casing dominates tip clearance flow just in the vicinity of the leading edge. At roughly about midchord, the flow exits tip clearance at the blade suction side and generates the tip clearance vortex.

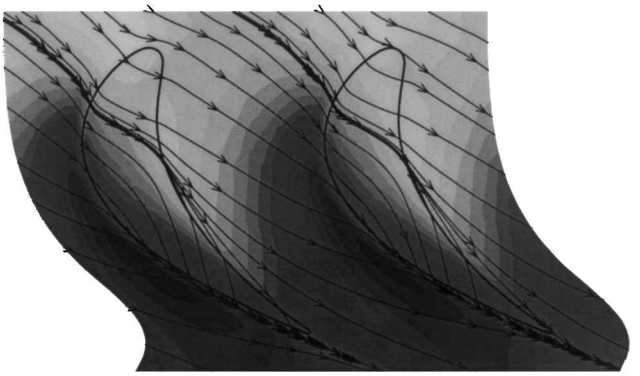

Fig. 7 Computed streamlines on pressure contours near the casing; relative frame of reference, rotor.

Figure 8 documents close agreement between computed and experimentally observed tip clearance flow. The trace of the suction side pressure trough clearly indicates the extension of the tip clearance vortex. The pressure plateau at midchord found experimentally is not predicted as the actual blade exhibits a sinking, by virtue of which the blade is mounted on the hub. It is interesting to note the disagreement of the currently predicted negative incidence and the experiment reported in Ref. 17. More recent experimental data support the computational findings.

Rotor/Stator Interaction

By virtue of the conservative sliding interface algorithm potential interaction as well as the influence of wakes on the downstream cascade, except for transition, are taken into account in the present investigation. Initially, time-dependent rotor/stator interaction caused by wakes is illustrated by the entropy. Here, the entropy is used as a relative quantity with different reference levels in different figures. Thereby, particle movement is indicated, as the transport of entropy is associated with the flow velocity.

Figure 9 depicts instantaneous entropy contours every quarter period. In compliance with analytical considerations, the entropy level raises continuously in streamwise direction. The tangential deflection of the viscous wake in the vicinity of the leading edges is evident, thereby illustrating potential interaction. Inside the rotor passage wakes are greatly affected by the prevailing pressure gradient. They undergo strong turning, interact with rotor boundary layers, and finally merge with the rotor wakes. Prior to merging, the stator wakes assume relative streamwise orientation inside the

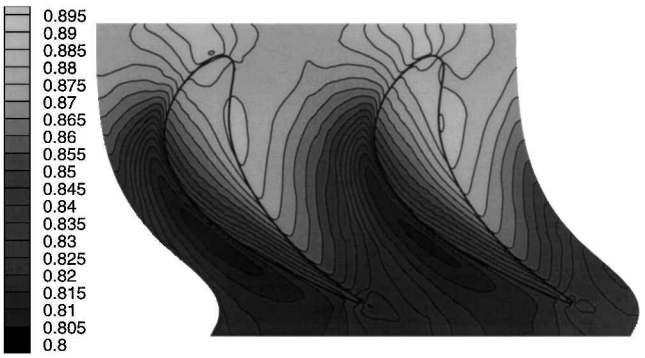

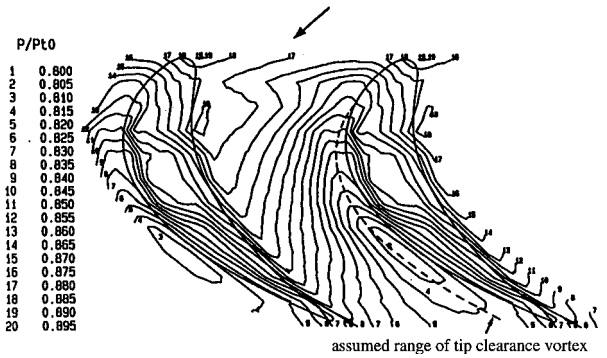

Fig. 8 Comparison between computed and experimentally observed casing pressure contours inside the rotor passage.[17]

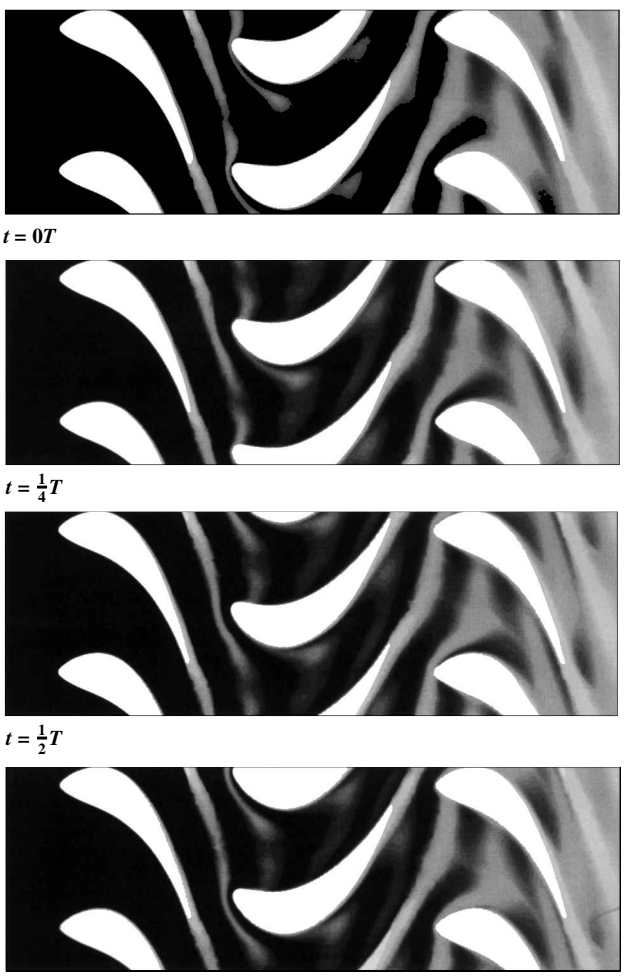

Fig. 9 Instantaneous entropy contours at midspan.

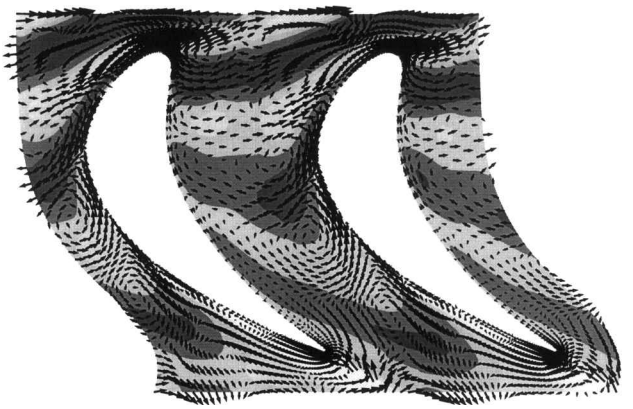

Fig. 10 Negative jet inside the rotor passage.

rotor cascade. Therefore, merging compromises the identification of stator and rotor wakes.

Inside the second stator mixing is enhanced by secondary flow features generated within the upstream cascades. Characteristics of the rotor wakes passing the second stator are similar to the rotor flow features though.

Inside the rotor and the stator blade passages, wakes are seen to exhibit inhomogeneous structures. At the suction sides a loss core is found, where losses undergo diffusive mixing near the pressure sides of the blades. The latter can be solely explained by a relative flow inside the moving wakes, e.g., the well-known negative jet. Figure 10 depicts secondary velocity vectors on entropy contours. Here, secondary velocity is defined as the vector difference between temporally averaged and instantaneous velocity. From Fig. 10 a secondary flow agglomerating losses close to the suction side is obvious. For equilibrium reasons secondary flow recirculates toward the blade pressure surface outside the moving wakes.

Figure 11 depicts the apparent existence of a local and transient maximum of the absolute total pressure caused by the rotor. The maximum is on the rotor blade suction side close to the leading edge. The existence of the local maximum (where total pressure is found to be higher than at inflow) can be supported from perturbations by upstream running acoustic waves. Indeed, the force field generated by the rotor can be felt upstream of the rotor. As the force field is moving (at a speed that is close to the convection velocity), it has the ability to locally feed the flowfield with energy, which accounts for an increase in total pressure even upstream of the rotor.

This implies that total pressure can be misleading in drawing conclusions in regard to loss-generating mechanisms. On the other hand, from Figs. 9 and 12 entropy is seen to be remarkably less subject to unsteadiness. As entropy is solely associated with the characteristic of particle movement, it can therefore be considered as a more elaborate quantity serving to understand unsteady loss generation.

At the rotor exit computations and experiments are compared using instantaneous Mach number contours (Fig. 13). The Mach-number field is seen to be well predicted except for the local Mach-number maximum near hub at $0T$. Because a physical explanation for this local instantaneous maximum may be purely academical, the near hub maximum is assumed to reflect the influence of different measuring techniques used in near-wall regions and in the bulk flow.

The amount of unsteadiness exerted on the rotor midspan pressure distribution is depicted in Fig. 14. The agreement is considered satisfactory, where it is emphasized that no code rerun using optimized boundary conditions was performed. Unsteadiness is about 1% of the time-averaged pressure and is found to be most pronounced on the suction side upstream of the midchord position.

Figure 15 depicts the entropy field at the second stator exit. Despite the obvious similarities with Fig. 12, a decrease in losses near shroud is found. Obviously, the first stator end-wall boundary layers

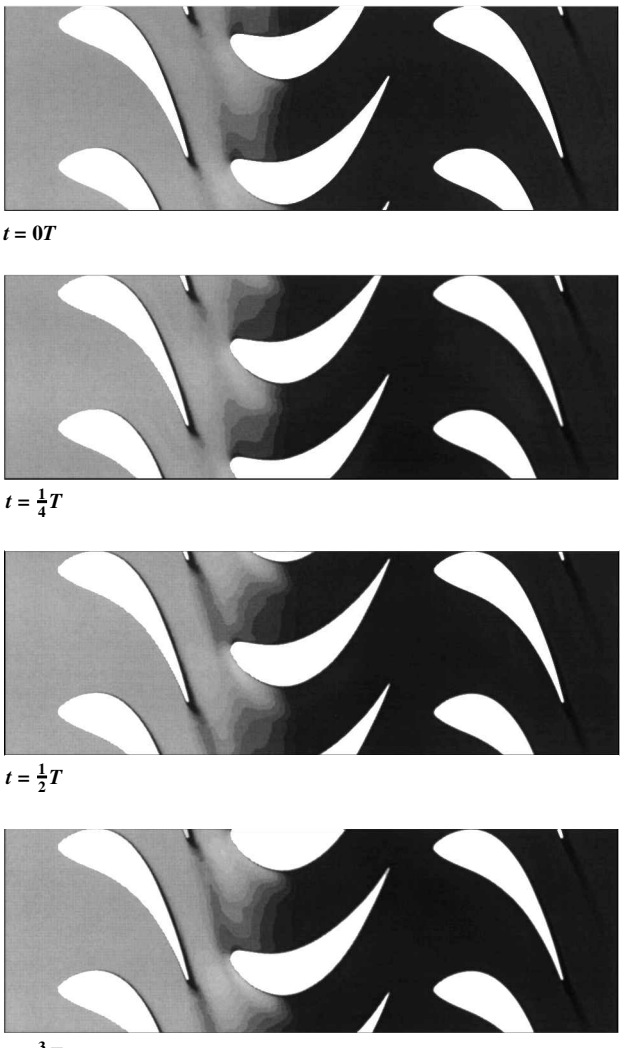

Fig. 11 Absolute total pressure at midspan.

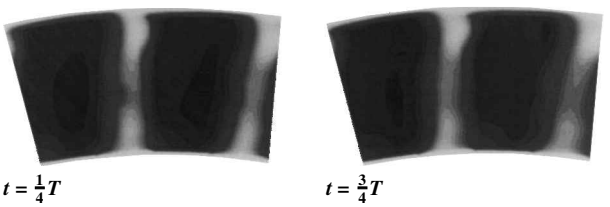

Fig. 12 Entropy at the first stator exit.

undergo an extended thickening process, whereas the rotor motion resets the end-wall boundary-layer growth.

At the second stator exit rotor losses migrate from the midpassage region at $0T$ to the left, where they intersect the stator wake at about $\frac{1}{2}T$–$\frac{3}{4}T$. The characteristic structure of the rotor loss regions in spanwise direction is preserved inside the successive stator, which is a clear indication for both blending and merging of rotor and stator loss generation. Here, the interaction of rotor-tip clearance flow and the passage vortex is found at roughly 75% span at the second stator exit.

Computed total pressure can be compared to experimental data at the stator exit by virtue of Fig. 16. Computational results apparently overpredict stator wake spreading. Data mismatch may be explained by two reasons. First, the computational grid density rapidly diminishes downstream of the blade trailing edge, and, therefore, resolution is insufficient. Second, because of finite probe sizes, the actual flow probing is located upstream of the distinct plane 3.

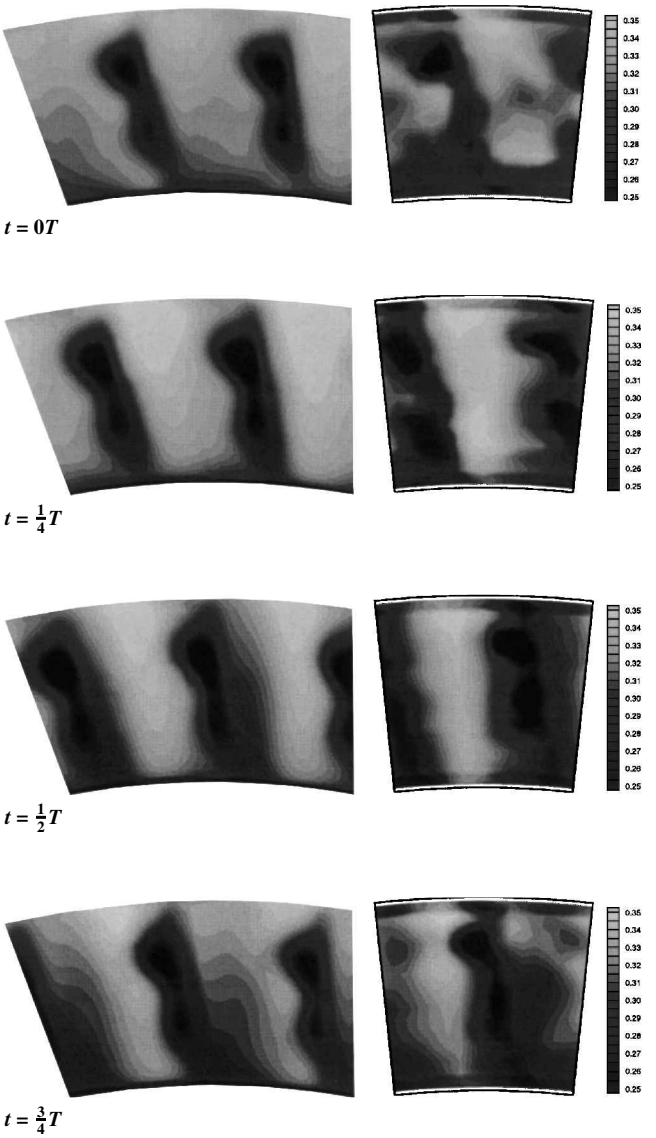

Fig. 13 Relative Mach number at rotor exit. Left column: computation; right column: experiment.[14]

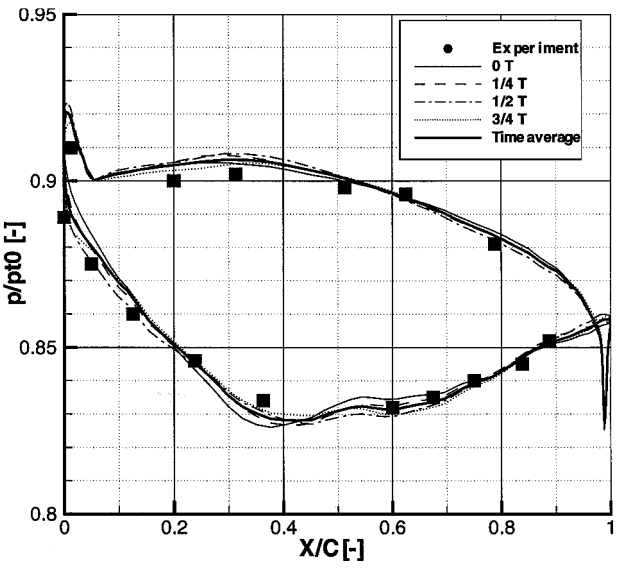

Fig. 14 Static pressure at rotor midspan.

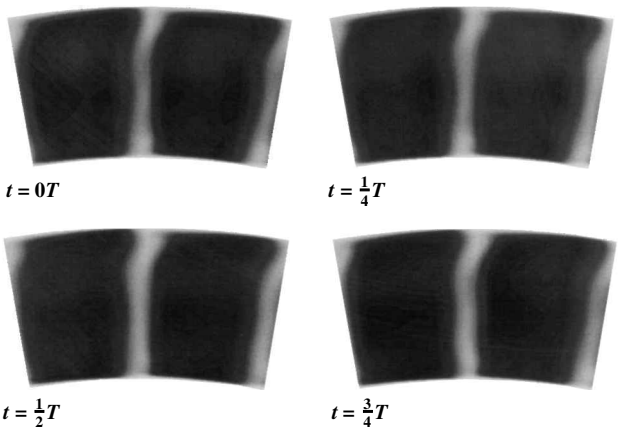

Fig. 15 Entropy contours at the second stator exit.

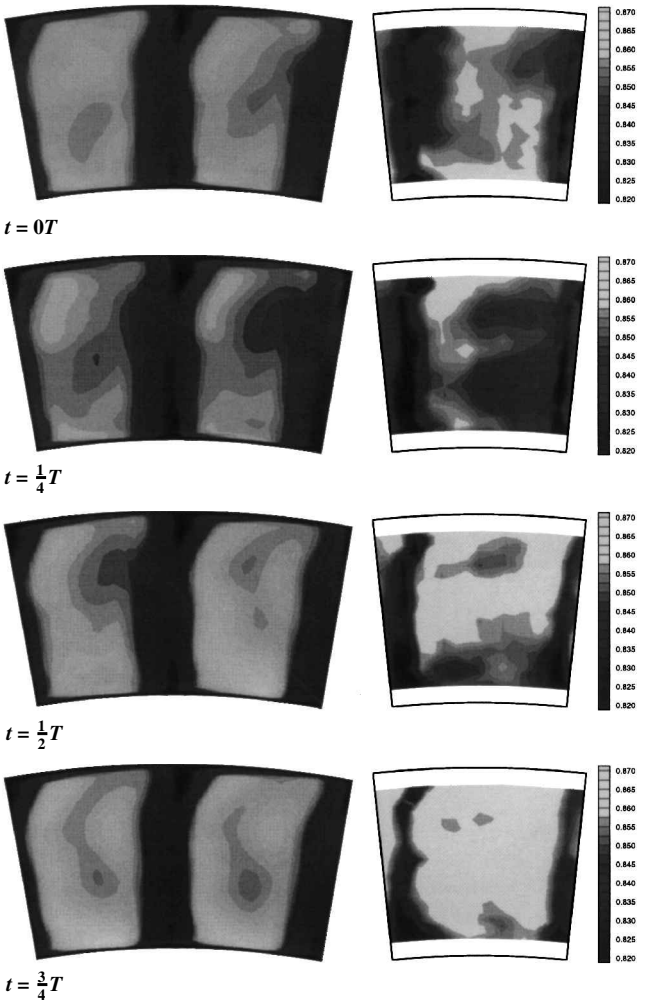

Fig. 16 Absolute total pressure at second stator exit. Left column: computation, right column: experiment.[14]

Therefore, the actual discrepancies between computational and experimental data are presumably less pronounced as depicted. The relative rotor wake motion is clearly seen, where the portion associated with tip clearance flow is about to pass the second stator wake at $0T$. Unfortunately, the low total pressure region at 30% span between $\frac{1}{4}T$ and $\frac{1}{2}T$ is not found in the computed results. On the other hand, there is evidence for significant contributions by transition, relaminarization, and laminar separation, which are not taken into consideration in the algorithm presented here.

Concluding Remarks

A three-dimensional Navier–Stokes code for the analysis of the flow in a multistage turbomachine has been developed by revision and extension of a single blade-row analysis code. The implicit algorithm allows physically motivated time steps rather than the use of a time step restricted by the Courant–Friedrichs–Lewy stability criterion. Space time periodicity is enforced according to the approach of Erdos et al.[13] The rotor-stator grid interface is treated with a partial-flux technique that is fully conservative.

Calculations were run for the ERCOFTAC subsonic axial turbine of the RWTH Aachen. The low subsonic turbine flow exhibits all kinds of vortical flow structures, which have been simulated numerically: passage vortices, horseshoe vortices, and tip clearance vortices. Numerical results enabled the analysis of interesting details of the flow, e.g., some concurrent effects in the rotor-tip clearance. Mass-averaged Mach numbers, total pressures, and yaw angles showed a very good agreement between computation and measurements. In regard to typical unsteady phenomena, entropy contour plots gave much information about the time evolution of wakes. The well-known negative jet was found to account for the local accumulation of high entropy material inside the wakes. For a faithful representation of losses on instantaneous plots, the entropy seems to be a more suitable quantity than the total pressure, as the latter was found to be highly sensitive to acoustic waves. In particular, it was shown how entropy contours in different blade-to-blade sections in the rotor, and in the second stator can give detailed information on the loss generation mechanisms.

Although numerical results are in good agreement with experimental data, it is still necessary to study the grid dependency of the solution. Moreover, computed results give rise to a strong incentive for further research in turbulence modeling with respect to laminar/turbulent transition.

Acknowledgments

The authors gratefully acknowledge sponsorship by the Bundesministerium für Forschung und Technologie for basic code development within the common german project AG-Turbo. The first author would like to express his gratitude to the Studienstiftung des Deutschen Volkes for sponsoring the extension to multistage analyses. The computations were carried out on a FUJITSU VPP 300 of the computer center of the Technical University of Aachen, Germany, and different workstation models, which have been made available to the institute by Hewlett-Packard GmbH, Germany. The fourth author expresses his gratitude to one year of support by the ICOMP/Ohio Aerospace Institute/NASA Lewis Research Center. Finally, all authors are indebted to R. E. Walraevens for accurately providing massive experimental data.

References

[1]Hodson, H. P., "An Inviscid Blade-to-Blade Prediction of Wake-Generated Unsteady Flow," *Journal of Engineering for Power*, Vol. 107, 1985, pp. 337–344.

[2]Galpin, P. F., Broberg, R. B., and Hutchinson, B. R., "Three-Dimensional Navier Stokes Predictions of Steady State Rotor/Stator Interaction with Pitch Change," *Proceedings of CFD 95, 3rd Annual Conference of the CFD Society of Canada*, Banff, Canada, Vol. 1, 1995.

[3]Adamczyk, J. J., Chen, J. P., and Celestina, M. L., "A New Procedure for Simulating Unsteady Flows Through Turbomachinery Blade Passages," American Society of Mechanical Engineers, Paper 94-GT-151, 1994.

[4]Mylonas, J., "Unsteady 2D Flow Calculation in Turbomachinery," *Proceedings of the 4th International Symposium on Unsteady Aerodynamics and Aeroelasticity of Turbomachines and Propellers*, Aachen, Germany, Sept. 1987.

[5]Saxer, A. P., and Giles, M. B., "Predictions of 3-D Steady and Unsteady Inviscid Transsonic Stator/Rotor Interaction with Inlet Radial Temperature Non-Uniformity," American Society of Mechanical Engineers, Paper 93-GT-10, 1993.

[6]Dawes, W. N., "Simulating Unsteady Turbomachinery Flows on Unstructured Meshes Which Adapt Both in Time and Space," American Society of Mechanical Engineers, Paper 93-GT-104, 1993.

[7]Benetschik, H., Lohmann, A., Lücke, J., and Gallus, H., "Inviscid and Viscous Analysis of Three-Dimensional Turbomachinery Flows Using an Implicit Upwind Algorithm," AIAA Paper 96-2556, July 1996.

[8]Chien, K.-Y., "Predictions of Channel and Boundary-Layer Flows with a Low-Reynolds-Number Turbulence Model," *AIAA Journal*, Vol. 20, No. 1, 1982, pp. 33–38.

[9]Kato, M., and Launder, B. E., "The Modeling of Turbulent Flow Around Stationary and Vibrating Square Cylinders," 9th Turbulent Shear Flow Symposium, Kyoto, 1993.

[10]Roe, P. L., "Approximate Riemann Solvers, Parameter Vectors and Difference Schemes," *Journal of Computational Physics*, Vol. 43, 1981, pp. 357–372.

[11]Chakravarthy, S., "High Resolution Upwind Formulations for the Navier–Stokes Equations," Von Kárman Institute for Fluid Dynamics Lecture Series 1988-05, 1988.

[12]Rai, M. M., "Unsteady Three-Dimensional Navier–Stokes Simulations of Turbine Rotor-Stator Interaction," AIAA Paper 87-2058, June–July 1987.

[13]Erdos, J. I., Alzner, E., and McNally, W., "Numerical Solution of Periodic Transonic Flow Through a Fan Stage," *AIAA Journal*, Vol. 15, No. 11, 1977, pp. 1565–1571.

[14]Walraevens, R. E., and Gallus, H. E., "Testcase 6: 1-1/2 Stage Axial Flow Turbine," ERCOFTAC SIG on Three-Dimensional Turbomachinery Flow Prediction, Les Arcs, France, Jan. 1995.

[15]Walraevens, R. E., Gallus, H. E., Jung, A. R., Mayer, J. F., and Stetter, H., "Experimental and Computational Study of the Unsteady Flow in a 1.5 Stage Axial Turbine with Emphasis on the Secondary Flow in the Second Stator," American Society of Mechanical Engineers, 43rd ASME Gas Turbine and Aeroengine Congress, Stockhom, 1995.

[16]Stephan, B., and Walraevens, R. E., "FVV-Forschungsvorhaben: Turbinenlaufrad/-leitradströmung II," Tischvorlage zur 3. Sitzung des FVV-Arbeitskreises Turbinenlaufrad/-leitradströmung II, 1997.

[17]Zeschky, J., "Experimentelle Untersuchung der Dreidimensionalen Instationären Rotorströmung Einer Axialen Kaltlufturbine," Ph.D. Dissertation, Rheinisch Westfälische Technische Hochschule Aachen, Germany, July 1991.